J. Fluid Mech. (1994), *vol.* 261, *pp.* 199–222

The motion of particles in the Hele-Shaw cell

By C. POZRIKIDIS

Department of Applied Mechanics and Engineering Sciences, University of California at San Diego, La Jolla, CA 92093-0411, USA

(Received 11 February 1993 and in revised form 24 August 1993)

The force and torque on a particle that translates, rotates, or is held stationary in an incident flow within a channel with parallel-sided walls, are considered in the limit of Stokes flow. Assuming that the particle has an axisymmetric shape with axis perpendicular to the channel walls, the problem is formulated in terms of a boundary integral equation that is capable of describing arbitrary three-dimensional Stokes flow in an axisymmetric domain. The method involves: (*a*) representing the flow in terms of a single-layer potential that is defined over the physical boundaries of the flow as well as other external surfaces, (*b*) decomposing the polar cylindrical components of the velocity, boundary surface force, and single-layer potential in complex Fourier series, and (*c*) collecting same-order Fourier coefficients to obtain a system of one-dimensional Fredholm integral equations of the first kind for the coefficients of the surface force over the traces of the natural boundaries of the flow in an azimuthal plane. In the particular case where the polar cylindrical components of the boundary velocity exhibit a first harmonic dependence on the azimuthal angle, we obtain a reduced system of three real integral equations. A numerical method of solution that is based on a standard boundary element-collocation procedure is developed and tested. For channel flow, the effect of domain truncation on the nature of the far flow is investigated with reference to plane Hagen–Poiseuille flow past a cylindrical post. Numerical results are presented for the force and torque exerted on a family of oblate spheroids located above a single plane wall or within a parallel-sided channel. The effect of particle shape on the structure of the flow is illustrated, and some novel features of the motion are discussed. The numerical computations reveal the range of accuracy of previous asymptotic solutions for small or tightly fitting spherical particles.

1. Introduction

Particle motions in viscous flows are encountered in a broad range of natural, engineering, and biomedical applications, and their study has spawned a large body of theoretical and computational research. Early studies are reviewed by Happel & Brenner (1983) and Clift, Grace & Weber (1978), and more recent developments are discussed by Kim & Karrila (1991). One class of studies have considered the mobility problem where the main objective is to evaluate the linear and angular velocity of a particle that moves under the influence of a specified force or torque, as well as the complementary resistance problem whose objective is to evaluate the force and torque exerted on a particle that moves in a specified manner. Other studies are concerned with the structure of shear flow past particles with an objective to study the kinematics of the flow and evaluate the effective stresses in a suspension of particles regarded as a homogeneous medium.

The particular problem of interest in this paper is the motion of particles in an

infinite channel with parallel plane walls, known as the Hele-Shaw cell. We are interested in computing the force and torque exerted on a particle that (*a*) translates or rotates in an otherwise quiescent fluid, or (*b*) is held stationary in an incident linear or parabolic flow. These results are prerequisite for calculating the trajectories and residence times of particles that move under the influence of a specified force or torque, or are freely convected in plane Couette or plane Poiseuille flow.

Interest in particle motions in the Hele-Shaw cell is motivated by two areas of application. The first area concerns the coating of liquids in the manufacturing of photographic films and magnetic tapes, by means of the slide coating method. In this method, the liquid to be coated is supplied into a narrow channel, which is part of the coating die, it exits the channel, flows down an inclined slide, and is then transferred onto a moving substratum. Often, owing to fluctuations in manufacturing conditions and material imperfections, the coated liquid contains impurities in the form of gel agglomerates and air bubbles. These particles introduce flow disturbances that are responsible for coating non-uniformities. Computing the residence time of the particles and the associated disturbance flow within the coating die is necessary for controlling the operation of the die and for improving the overall design of the coating process (Vrahopoulou 1992).

The second area of application concerns the motion of red blood cells through certain biological media. One example is blood flow through the flattened capillary network separating adjacent alveoli, the smallest units of space in the lung, called the interalveoral septum (Fung 1984). The flow channel is comprised of two parallel interalveoral walls that are held apart by a two-dimensional array of avascular septal posts. The blood cells move within the alveoral vascular space between the interalveoral walls, swinging to left and right in order to avoid the intercepting avascular posts. At the arterioral level, the thickness of the interalveoral septum may be as low as two or three times the cell diameter. As a first step towards assessing the residence time of blood cells in the interalveoral septum, we consider their convection velocity in plane Poiseuille flow, neglecting the presence of the posts. Another related application concerns the motion of red blood cells through the spleen and the bone marrow (Halpern & Secomb 1992). In the spleen, red blood cells move through venous sinuses; aged cells cannot withstand the developing shear stresses, break up, and are thus removed from the circulatory system.

There are a number of previous studies of particle motions in Stokes flow in the presence of one or two parallel walls. Series solutions in bipolar coordinates and asymptotic solutions for small particle-wall spacings are available for flow due to a sphere executing rigid-body motion above a plane wall, as well as for shear flow past a stationary sphere (see Goldman, Cox & Brenner 1967*a*, *b*; O'Neill & Stewartson 1967, and references therein). The corresponding flows for toroidal particles, prolate and oblate spheroids, and biconcave disks, were studied by Wakiya (1959), Kucaba-Pietal (1986), and Hsu & Ganatos (1989) using boundary integral and singularity methods. Ganatos *et al.* (1980*a*, *b*, 1982) considered the flow around a spherical particle and the motion of a settling or freely suspended particle between two parallel walls, and compared their results to those predicted by previous asymptotic solutions for small particles, obtained using the method of reflections. De Mestre (1973) considered the motion of a slender cylinder placed midway between two parallel plates, and Halpern & Secomb (1991) considered the motion of tightly-fitting disk-shaped particles in a parallel-sided channel. The former is based on the method of reflections, and the latter on the theory of lubricating flow. A number of other authors have considered the flow about, and the motion of, solitary or arrays of two-dimensional

(cylindrical) particles placed between two parallel plates (see Dvinski & Popel 1987*a*, *b*; Zhou & Pozrikidis 1993).

One goal of the present paper is to illustrate the motion of non-spherical particles with emphasis on investigating the significance of particle shape, size, and aspect ratio. To this end, we note that oblate and disk-like shapes are of particular bioengineering importance, as they provide good approximations to the shapes assumed by red blood cells during flow through closely-spaced plates (Halpern & Secomb 1992).

The well-established numerical efficiency and flexibility of the boundary integral method makes it a strong candidate for tackling the present problem. The standard boundary integral formulation reduces the problem of computing a three-dimensional creeping flow to solving a Fredholm integral equation of the first kind for the distribution of the traction over the surface of the particle as well as all other boundaries of the flow (Pozrikidis 1992). Alternative formulations leading to integral equations of the second kind that are amenable to iterative solutions are discussed by Kim & Karrila (1991) and Pozrikidis (1992). The application of these primary methods to study particle motions in a channel yields a set of two-dimensional integral equations defined over the walls of the channel and the particle surface. Unfortunately, an accurate numerical solution requires discretizing three-dimensional boundaries of infinite extent, and yields a large system of linear algebraic equations whose solution demands a prohibitively large amount of computational effort. In the context of the present paper, these difficulties are compounded by the fact that, in general, the flow due to a particle in a parallel-sided channel decays at an algebraic rate, thus requiring a large domain for numerical computation.

In this study, the efficiency of the boundary integral method is critically improved by considering axisymmetric particle shapes with axis perpendicular to the walls of the channel, but placed at an arbitrary position across the channel. Under these circumstances, all boundaries of the flow, including the particle surface and the walls of the channel, are axisymmetric with respect to the particle axis. This allows the Fourier decomposition of all flow variables involved in the boundary integral representation with respect to the common azimuthal angle. Separating same-order Fourier coefficient yields a system of one-dimensional integral equations of the first kind over the trace of the boundaries in an azimuthal plane. The crucial benefit is that the dimension of the computational problem is reduced by two units with respect to the dimension of the physical problem. Thus, computing a three-dimensional flow requires solving a system of one-dimensional integral equations, and this allows for extensive and accurate numerical investigations. In the special case where the boundary conditions for the polar cylindrical components of the velocity exhibit a first harmonic dependence on the azimuthal angle, we obtain three one-dimensional integral equations over the trace of each boundary in an azimuthal plane.

The particular implementation of the boundary integral method developed in this paper proceeds by expressing the flow in terms of a single-layer potential, and then implementing Fourier decompositions to obtain a system of one-dimensional integral equations for the Fourier coefficients of the boundary surface force. The single-layer representation is carried out in a natural manner that preserves the identity of the surface force in the single-layer potential over the physical boundaries of the flow. This computational formalism is applicable to a broad range of problems of engineering interest, apart from the one considered in this study, and some examples are illustrated in § 2. In a companion paper, the method is applied to study shearing flow over a plane wall containing an axisymmetric cavity or a circular pore (Pozrikidis 1994).

The present boundary integral method is related to that developed by Hsu &

Ganatos (1989) to compute the motion of axisymmetric particles above a plane wall. Their method begins with the standard boundary integral formulation for rigid-body motion, involving the single-layer potential alone and employing the Green's function for flow in a semi-infinite domain bounded by a rigid plane wall, and introduces Fourier–Legendre expansions for the surface force over the particle surface to obtain a system of algebraic equations for the coefficients in the expansions. Their method has a more general applicability than the present method, in the sense that it is capable of accommodating inclined particle orientations, at the expense, however, of considerable analytical complexity. One disadvantage is that the method of Hsu & Ganatos (1989) is less amenable to accommodating more general boundary shapes. Furthermore, the presently developed single-layer representation complements the completed double-layer representation developed by Kim & Karrila (1991) and Pozrikidis (1992). The relationship between the two methods will be discussed briefly in §2 of this paper.

In §2 we present the boundary integral formulation, illustrate its range of application, discuss its implementation, and develop a numerical method of solution that is based on a standard low-order discretization followed by pointwise collocation. The numerical results suggest that the method is well-posed and numerically stable, which means that high accuracy is achieved with moderate computational resources.

In §3 we consider the motion of oblate spheroids above a single plane wall, with a main objective to demonstrate the accuracy of the numerical method by comparing the numerical results with available exact and numerical solutions. Apart from establishing a point of reference, these results reveal some interesting new behaviours.

In §4 we consider flow in a Hele-Shaw cell past a cylindrical post, with a main objective to investigate the application of the boundary integral method to channel flow. We study the numerical implementation of the far-field boundary condition on the truncated computational domain, and illustrate its significance on the drag force exerted on the channel walls owing to the presence of the post.

In §5 we study the motion of oblate spheroids and the flow past oblate spheroids in the Hele-Shaw cell. We outline the implementation of the boundary integral method, present numerical results for particles placed at the centre and off the centre of the channel, and discuss the effect of the particle shape on the particle motion and structure of the flow.

In summary, our objectives in this paper are twofold. First, to develop and implement an efficient boundary integral method that is suitable for computing general three-dimensional flows in axisymmetric domains. Secondly, to provide accurate information on the motion of non-spherical particles in the Hele-Shaw channel.

2. A boundary integral method for Stokes flow in axisymmetric domains

We consider an arbitrary three-dimensional flow at vanishing Reynolds numbers, governed by the Stokes equation and the continuity equation. We select an arbitrary control volume in the domain of flow, bounded by a set of open or closed surfaces S, and apply the standard boundary integral formulation to obtain an expression for the velocity at a point $\boldsymbol{x}_0$ located within the control in terms of two boundary distributions of singular solutions to the governing equations, called the single-layer and double-layer hydrodynamic potential, respectively, in the form

$$\boldsymbol{u}(\boldsymbol{x}_0) = -\frac{1}{8\pi\mu} \boldsymbol{I}^s(\boldsymbol{x}_0; \boldsymbol{f}, S) + \frac{1}{8\pi} \boldsymbol{I}^d(\boldsymbol{x}_0; \boldsymbol{u}, S) \tag{2.1}$$

(Pozrikidis 1992). Here $\boldsymbol{f}$ is the boundary surface force or traction defined as $\boldsymbol{f} = \boldsymbol{\sigma} \cdot \boldsymbol{n}$,

$\boldsymbol{\sigma}$ is the stress tensor, and $\boldsymbol{n}$ is the unit normal vector pointing into the control volume. The hydrodynamic potentials shown in (2.1) have the explicit forms

$$I_i^s(\boldsymbol{x}_0;\boldsymbol{f},S) = \int_S G_{ij}(\boldsymbol{x}_0,\boldsymbol{x}) f_j(\boldsymbol{x})\,\mathrm{d}S(\boldsymbol{x}), \tag{2.2}$$

and

$$I_i^d(\boldsymbol{x}_0;\boldsymbol{u},S) = \int_S u_j(\boldsymbol{x})\, T_{jik}(\boldsymbol{x},\boldsymbol{x}_0)\, n_k(\boldsymbol{x})\,\mathrm{d}S(\boldsymbol{x}) \tag{2.3}$$

(Pozrikidis 1992). $\boldsymbol{G}$ and $\boldsymbol{T}$ are, respectively, Green's functions of the equations of Stokes flow for the velocity and stress. The free-space Green's functions, representing the velocity and stress due to a point force in an infinite fluid, are given by

$$G_{ij}(\boldsymbol{x}_0,\boldsymbol{x}) = \frac{\delta_{ij}}{|\hat{\boldsymbol{x}}|} + \frac{\hat{x}_i \hat{x}_j}{|\hat{\boldsymbol{x}}|^3}, \quad T_{jik}(\boldsymbol{x}_0,\boldsymbol{x}) = -6\frac{\hat{x}_j \hat{x}_i \hat{x}_k}{|\hat{\boldsymbol{x}}|^5}, \tag{2.4}$$

where $\hat{\boldsymbol{x}} = \boldsymbol{x} - \boldsymbol{x}_0$. Equation (2.1) may be used to compute the flow field at a point $\boldsymbol{x}_0$ located within the control volume, from knowledge of the distributions of the velocity $\boldsymbol{u}$ and surface force $\boldsymbol{f}$ over the set of boundaries S. If we apply (2.1) at a point $\boldsymbol{x}_0$ that is located outside the control volume, we will find that the right-hand side is equal to zero (Pozrikidis 1992, chap. 2).

The starting point in developing the present boundary integral formulation involves eliminating the double-layer potential from the general representation (2.1). In the particular case of (*a*) flow due to a moving rigid body or, (*b*) incident flow $\boldsymbol{u}^\infty$ past a body executing rigid-body motion, the elimination may be effected in a natural manner that preserves the exact form of the single-layer potential yielding, respectively,

$$\boldsymbol{u}(\boldsymbol{x}_0) = -\frac{1}{8\pi\mu} I^s(\boldsymbol{x}_0;\boldsymbol{f},S_B), \quad \boldsymbol{u}(\boldsymbol{x}_0) = \boldsymbol{u}^\infty(\boldsymbol{x}_0) - \frac{1}{8\pi\mu} I^s(\boldsymbol{x}_0;\boldsymbol{f},S_B). \tag{2.5}$$

Here, with the use of an appropriate Green's function, the set S was reduced to the surface of the body S_B alone (Pozrikidis 1992, chapter 2).

Under more general circumstances, the single-layer potential may be eliminated by introducing extraneous single-layer distributions over surfaces that are located outside the control volume. One such elimination will be described in §4 with reference to flow in the Hele-Shaw cell past a cylindrical post. The final outcome is an expression for the velocity in the form

$$\boldsymbol{u}(\boldsymbol{x}_0) = \boldsymbol{u}^\infty(\boldsymbol{x}_0) - \frac{1}{8\pi\mu} \sum_{i=1}^{K} I^s(\boldsymbol{x}_0;\boldsymbol{f},D_i), \tag{2.6}$$

where D_i $(i = 1,2,\ldots,K)$, is a collection of open or closed subdomains that either belong to the set S, which contains all boundaries of the control volume, or are located outside the control volume. In the second case, the distribution of $\boldsymbol{f}$ over D_i is assumed to be known. The set of all D_i includes the set S. $\boldsymbol{u}^\infty$ represents a known incident flow.

Equation (2.6) applies at points $\boldsymbol{x}_0$ that are located within the control volume, as well as at points $\boldsymbol{x}_0$ located on any of the subdomains D_i that belong to the set S. Applying (2.6) at points on these subdomains, and specifying the boundary velocity, reduces (2.6) to a Fredholm integral equation of the first kind for the boundary distribution of the surface force $\boldsymbol{f}$. Solving this equation and substituting the solution back into (2.6) allows the computation of the velocity at any point within the control volume. These developments complete the formulation of the problem in terms of an integral equation of the first kind for the boundary surface force.

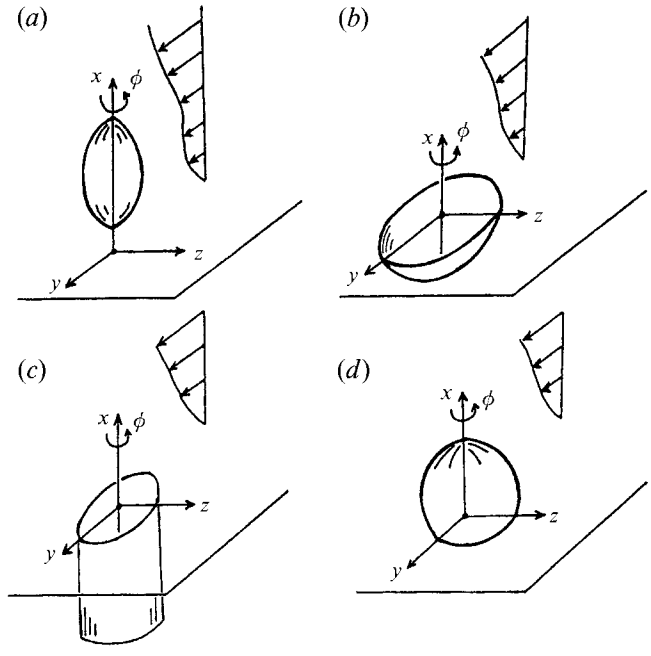

FIGURE 1. Examples of three-dimensional flows in axisymmetric domains. (*a*) Flow past an axisymmetric particle above a plane wall; the axis of the particle is perpendicular to the wall. (*b*) Shear flow over a plane wall with an axisymmetric cavity; the shape of the cavity may be a section of a sphere. (*c*) Shear flow over a plane wall with a cylindrical pore of finite or infinite depth. (*d*) Shear flow over a plane wall with an axisymmetric protrusion; the protrusion may represent a blood cell adhering to a vessel wall.

2.1. *Axisymmetric boundaries*

At this point, we confine our attention to flows that are bounded by axisymmetric surfaces. Examples include flow past an axisymmetric particle located above a plane wall, illustrated in figure 1(*a*), a flow over a plane wall with an axisymmetric cavity or a cylindrical pore of finite or infinite depth, illustrated in figures 1(*b*, *c*), and shearing flow over a plane wall with an axisymmetric protrusion such as a section of a sphere or a cylinder, illustrated in figure 1(*d*). Additional examples are flow in a Hele-Shaw cell past a cylindrical post, illustrated in figure 3(*a*), and flow past a particle in the Hele-Shaw cell illustrated in figure 4 (see also Pozrikidis 1994).

Expanding the polar cylindrical components of the velocity, boundary surface force, and single-layer potential, in complex Fourier series with respect to the azimuthal angle ϕ over each axisymmetric subdomain D_i, we obtain

$$\left.\begin{aligned} u_\alpha(x_0, \sigma_0, \phi_0) &= \sum_{n=-\infty}^{\infty} u_{\alpha n}(x_0, \sigma_0) \exp(in\phi_0), \quad f_\beta(l, \phi) = \sum_{n=-\infty}^{\infty} f_{\beta n}(l) \exp(in\phi), \\ I_\alpha^S(x_0, \sigma_0, \phi_0; f, D_i) &= \sum_{n=-\infty}^{\infty} \exp(in\phi_0) \int_{C_i} Q_{\alpha\beta n}(\hat{x}, \sigma, \sigma_0) f_{\beta n}\, \sigma \, \mathrm{d}l, \end{aligned}\right\} \tag{2.7}$$

where Greek indices stand for the polar cylindrical coordinates x, σ, or ϕ. Here C_i is the trace of the boundary D_i in the x, y azimuthal plane, l is the arclength around C_i, and repeated Greek but not Roman subscripts are summed over x, σ, and ϕ. The particular form of the matrix $Q_{\alpha\beta n}$ depends upon the choice of Green's function (Pozrikidis 1992, §2.4).

Substituting the Fourier series (2.7) into the boundary integral equation (2.6) and collecting same-order Fourier coefficients yields the following integral relation between the Fourier coefficients of the velocity and boundary surface force:

$$u_{\alpha n}(x_0, \sigma_0) = u^{\infty}_{\alpha n}(x_0, \sigma_0) - \frac{1}{8\pi\mu} \sum_{i=1,\ldots,K} \int_{C_i} Q_{\alpha\beta n}(\hat{x}, \sigma, \sigma_0) f_{\beta n}\, \sigma\, \mathrm{d}l. \tag{2.8}$$

Applying (2.8) at points located on the contours C_i corresponding to the physical boundaries of the flow comprising the set S, and requiring boundary conditions for the velocity, yields a system of Fredholm integral equations of the first kind for the unknown Fourier coefficients of the boundary surface force $f_{\beta n}$ over these C_i. The Fourier coefficients over the contours C_i that do not below to the set S are assumed to be known.

In summary, the two main steps that led us to the integral equation (2.8) are the representation of the flow in terms of a single-layer potential, and the Fourier expansion of all terms in the boundary integral equation.

Hsu & Ganatos (1989) obtained a system of equations similar to (2.8), applicable for the particular case of a particle moving above a plane wall, and then expanded $f_{\beta n}$ in Legendre series with respect to distance along the particle axis and performed the integrations analytically, thereby replacing the integral with a double sum.

Kim & Karrila (1991) developed an alternative formulation that begins by representing the flow in terms of the competed double-layer potential, and then proceeds by applying Fourier decompositions. This yields a set of integral equations of the second kind for the Fourier coefficients of the density of the double-layer potential. Comparing the single-layer to the double-layer formulation, we find that the former offers analytical simplicity and circumvents introducing artificial densities of hydrodynamic potentials. The double-layer formulation, however, has the important advantage that it allows for iterative solutions and, therefore, it is designated for flows with a multitude of boundaries, such as the flow past a collection of suspended particles.

2.2. *Boundary conditions with first-harmonic dependence on the azimuthal angle*

We now focus our attention further to situations in which the boundary conditions for the polar cylindrical components of the velocity exhibit first-harmonic dependence on the azimuthal angle, in the form

$$u_x = U_x(x)\cos\phi, \quad u_\sigma = U_\sigma(x)\cos\phi, \quad u_\phi = -U_\phi(x)\sin\phi, \tag{2.9}$$

where U_x, U_σ, and U_ϕ are three arbitrary real functions. In terms of the corresponding Fourier coefficients introduced in (2.7), we obtain

$$u_{x1} = u_{x(-1)} = \tfrac{1}{2}U_x(x), \quad u_{\sigma 1} = u_{\sigma(-1)} = \tfrac{1}{2}U_\sigma(x), \quad u_{\phi 1} = -u_{\phi(-1)} = \tfrac{1}{2}\mathrm{i}U_\phi(x), \tag{2.10}$$

where i is the imaginary unit; all other Fourier coefficients are equal to zero. Although at first sight they may appear quite specialized, conditions (2.9) are able to accommodate a broad class of flows, including the flows illustrated in figure 1(*a–d*). Equations similar to (2.9) and (2.10) are assumed to apply for the incident flow $\boldsymbol{u}^{\infty}$.

The linearity of (2.8) suggests that, correspondingly, all but the first-order Fourier coefficients $f_{\alpha n}$ vanish and, furthermore, it dictates setting

$$f_{x1} = f_{x(-1)} \equiv f_x, \quad f_{\sigma 1} = f_{\sigma(-1)} \equiv f_\sigma, \quad f_{\phi 1} = -f_{\phi(-1)} \equiv \mathrm{i}f_\phi, \tag{2.11}$$

where f_x, f_σ, and f_ϕ are three independent real functions. Relations (2.11) are equivalent to

$$f_x = 2f_x\cos\phi, \quad f_\sigma = 2f_\sigma\cos\phi, \quad f_\phi = -2f_\phi\sin\phi. \tag{2.12}$$

Substituting (2.10) and (2.11) into (2.8) and simplifying we obtain the following system of three scalar real integral equations of the first kind for the unknown Fourier coefficients of the surface force:

$$U_\alpha(x_0,\sigma_0) = U_\alpha^\infty(x_0,\sigma_0) - \frac{1}{4\pi\mu}\sum_{i=1,\ldots,K}\int_{C_i} \Phi_{\alpha\beta}(\hat{x},\sigma,\sigma_0)\not{f}_\beta(x,\sigma)\,\sigma\,\mathrm{d}l(x). \tag{2.13}$$

Adopting the free-space Green's function given in (2.4), we find that the kernel $\boldsymbol{\Phi}$ is given by

$$\Phi_{\alpha\beta} = \begin{bmatrix} I_{11}+\hat{x}^2 I_{31} & \hat{x}(\sigma I_{31}-\sigma_0 I_{32}) & \hat{x}\sigma_0(I_{32}-I_{30}) \\ \hat{x}(\sigma I_{32}-\sigma_0 I_{31}) & I_{12}+(\sigma_0^2+\sigma^2)I_{32}-\sigma\sigma_0(I_{33}+I_{31}) & I_{10}-I_{12}+\sigma_0^2(I_{30}-I_{32})-\sigma\sigma_0(I_{31}-I_{33}) \\ \hat{x}\sigma(I_{30}-I_{32}) & I_{10}-I_{12}+\sigma^2(I_{30}-I_{32})-\sigma\sigma_0(I_{31}-I_{33}) & I_{12}+\sigma\sigma_0(I_{31}-I_{33}) \end{bmatrix} \tag{2.14}$$

where $\hat{x} = x - x_0$, and

$$I_{mn}(\hat{x},\sigma,\sigma_0) \equiv \int_0^{2\pi} \frac{\cos^n\omega}{[\hat{x}^2+\sigma^2+\sigma_0^2-2\sigma\sigma_0\cos\omega]^{\frac{1}{2}m}}\,\mathrm{d}\omega$$

$$= \frac{4k^m}{(4\sigma\sigma_0)^{\frac{1}{2}m}}\int_0^{\frac{1}{2}\pi} \frac{(2\cos^2\omega-1)^n}{(1-k^2\cos^2\omega)^{\frac{1}{2}m}}\,\mathrm{d}\omega, \tag{2.15}$$

with

$$k^2 = \frac{4\sigma\sigma_0}{\hat{x}^2+(\sigma+\sigma_0)^2}. \tag{2.16}$$

The integrals on the right-hand side of (2.15) may be expressed in terms of complete elliptic integrals of the first and second kind which, in turn, may be computed using either iterative methods or polynomial approximations (Pozrikidis 1992, chap. 2).

Once the solution to (2.13) is found, the y-component of the force and the z-component of the torque exerted on the boundary D_i are computed by contour integration as

$$F_y = 2\pi\int_{C_i}(\not{f}_\sigma+\not{f}_\phi)\,\sigma\,\mathrm{d}l, \tag{2.17}$$

and

$$T_z = 2\pi\int_{C_i}[x(\not{f}_\sigma+\not{f}_\phi)-\sigma\not{f}_x]\,\sigma\,\mathrm{d}l. \tag{2.18}$$

2.3. *Numerical solution of the integral equation*

The problem is reduced to solving the system of three Fredholm integral equations of the first kind shown in (2.13) for the unknown Fourier coefficient vector f over selected contours C_i. For this purpose, we discretize each contour C_i into a set of boundary elements that are either straight segments or circular arcs, assume that f is constant over each element, and apply (2.13) at the midpoint of each element to obtain a system of linear equations for the values f over all elements. This procedure yields a second-order accurate numerical method with respect to the number of boundary elements. The distribution of the element size is adjusted so as to provide us with adequate resolution at regions where the solution exhibits sharp variations.

The kernel of the integral equation, $\boldsymbol{\Phi}$, shows logarithmic singularities at the collocation points. Specifically, as $\boldsymbol{x}$ tends to $\boldsymbol{x}_0$, the off-diagonal components of $\boldsymbol{\Phi}$ exhibit a regular behaviour, but the diagonal components $\Phi_{xx}, \Phi_{\sigma\sigma}, \Phi_{\phi\phi}$ behave in a singular manner as $-2\ln r$, $-2\ln r$, and $-4\ln r$, where $r = |\boldsymbol{x}-\boldsymbol{x}_0|$. To compute the

singular boundary integrals with sufficient accuracy, we subtract-off the singular logarithmic contributions and then integrate them analytically over each singular element. The non-singular and regularized boundary integrals are computed using the six-point Gauss–Legendre quadrature.

To validate the numerical procedure we carried out a number of test computations. In one case we considered the translation and rotation of oblate spheroids along or about a major axis in infinite fluid, and obtained excellent agreement with the known exact analytical solution (the boundary integral formulation for this flow will be discussed in §3). In another case we considered simple shear flow $\boldsymbol{u} = (0, kx, 0)$ past a stationary spherical particle, where k is the shear rate, and found excellent agreement with the exact solution which is given by $\mathscr{F} = \mu k/(2a)[\sigma, 4x, 4x]$. In all cases the convergence of the numerical solution was confirmed to be quadratic. Additional tests of accuracy and further considerations of the numerical method will be presented in subsequent sections.

3. Oblate spheroids above a single plane wall

As a first step toward studying particle motions in a channel, we consider flow in the presence of a single plane wall, illustrated in figure 2(*a*). We are interested in computing the force and torque exerted on an axisymmetric particle that either translates along the y-axis or rotates around an axis that passes through its centre and is parallel to the z-axis. In addition, we are interested in computing the force and torque exerted on a particle that is held stationary in an incident simple shearing flow along the y-axis, as shown in figure 2(*a*). These results will serve to demonstrate the accuracy of the numerical method, but in addition, they will reveal certain new physical features of the flow regarding the effect of particle shape.

Following established notation, we express the force and torque exerted on a particle that translates along the y-axis with velocity V in terms of dimensionless resistance coefficients F^T and T^T as

$$\boldsymbol{F} = -6\pi\mu a V F^T \boldsymbol{j}, \quad \boldsymbol{T} = 8\pi\mu a^2 V T^T \boldsymbol{k}, \tag{3.1}$$

where a is the major axis of the generating ellipse, and $\boldsymbol{j}, \boldsymbol{k}$ are, respectively, the unit vectors in the y- and z-directions. The superscript T stands for 'translation'.

Similarly, we express the force and torque exerted on a particle that rotates about an axis that passes through its centre and is parallel to the z-axis with angular velocity Ω as

$$\boldsymbol{F} = 6\pi\mu a^2 \Omega F^R \boldsymbol{j}, \quad \boldsymbol{T} = -8\pi\mu a^3 \Omega T^R \boldsymbol{k}. \tag{3.2}$$

The superscript R stands for 'rotation'.

For a particle that is held stationary in the incident shear flow $\boldsymbol{u} = (0, kx, 0)$ we write

$$\boldsymbol{F} = 6\pi\mu a l k F^S \boldsymbol{j}, \quad \boldsymbol{T} = 4\pi\mu a^3 k T^S \boldsymbol{k}, \tag{3.3}$$

where l is the distance of the particle centre from the wall. The superscript S stands for 'shear flow'.

Not all of the above drag coefficient are independent; the reciprocal theorem for Stokes flow requires that $F^R = \frac{4}{3}T^T$ (Pozrikidis 1992, chap. 1). In the absence of the wall, the coefficients T^T and F^R are equal to zero, and $F^S = -F^T$, $T^S = -T^R$.

3.1. *Boundary integral formulation and computation of forces and torques*

Considering first flow due to a particle that translates along the y-axis with velocity V or rotates around an axis that passes through its centre and is parallel to the z-axis with angular velocity Ω, we begin with the single-layer representation given by the first

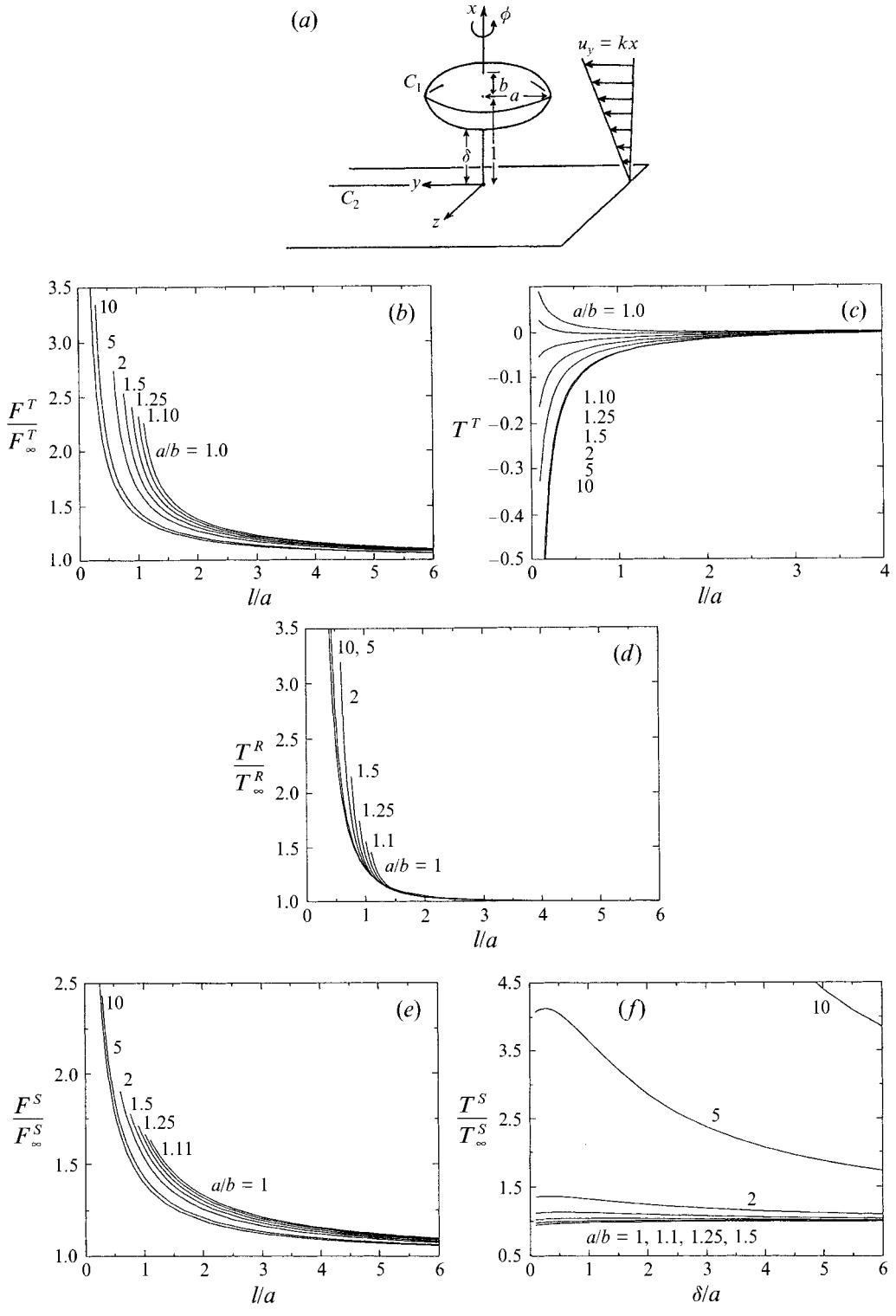

FIGURE 2. (*a*) Schematic illustration of an oblate spheroid located above a plane wall with axis perpendicular to the wall. Drag coefficients for: (*b*, *c*) translation, (*d*) rotation, and (*e*, *f*) shear flow, plotted with respect to particle elevation or wall-particle gap. The subscript ∞ designates the respective coefficients for unbounded flow.

equation in (2.5) and arrive at the integral equation (2.13) with two boundary contours: the trace of the particle C_1, and the trace of the wall C_2 in the $\phi = 0$ azimuthal plane which lies in the x, y-plane. The incident flow vanishes.

In the case of translation we require $u_x = 0, u_y = V, u_z = 0$ on the particle surface, yielding $U_x = 0, U_\sigma = V, U_\phi = V$. In the case of rotation we require

$$u_x = -\Omega y, u_y = \Omega(x-l), u_z = 0$$

on the particle surface, yielding $U_x = -\Omega\sigma(x), U_\sigma = \Omega(x-l), U_\phi = \Omega(x-l)$, where the notation $\sigma(x)$ emphasizes that, on the surface of the particle, σ is a function of x. In both cases of translation and rotation we require $U_x = U_\sigma = U_\phi = 0$ over the wall.

For unidirectional flow along the y-axis past a stationary particle, $\boldsymbol{u}^\infty = [0, V(x), 0]$, we begin with the single-layer representation, given by the second equation in (2.5), and arrive at (2.13) with the two contours C_1 and C_2 mentioned above. On the surface of the particle we require that the velocity vanishes. Introducing the disturbance flow $\boldsymbol{u}^D \equiv \boldsymbol{u} - \boldsymbol{u}^\infty$ we write

$$\boldsymbol{u} = 0 \text{ or } \boldsymbol{u}^D = -\boldsymbol{u}^\infty = [0, -V(x), 0],$$

yielding $U_x^D = 0, U_\sigma^D = -V(x), U_\phi^D = -V(x)$, where the superscript D stands for 'disturbance'. For a simple shear flow, $V(x) = kx$, where k is the shear rate.

In the case of translation and rotation, the force and torque exerted on the particle are computed using (2.17) and (2.18). In the case of shear flow past a stationary particle, we use the reciprocal theorem for Stokes flow to obtain the force and torque in terms of the distributions of the surface force on the particle for rigid-body motion, using the equations

$$\boldsymbol{F}^{\text{Shear flow}} = -\frac{4\pi k}{V}\int_{C_1}(\not{f}_\sigma^T + \not{f}_\phi^T)\, x\sigma\, \mathrm{d}l\boldsymbol{j}, \quad \boldsymbol{T}^{\text{Shear flow}} = -\frac{4\pi k}{\Omega}\int_{C_1}(\not{f}_\sigma^R + \not{f}_\phi^R)\, x\sigma\, \mathrm{d}l\boldsymbol{k}, \tag{3.4}$$

where the superscripts T and R designate 'translation' and 'rotation'. Using (3.4) bypasses the explicit computation of the shear flow and serves as an independent check of the accuracy of the computations.

3.2. *Results and discusion for oblate spheroids*

We carried out a series of computations with 32 and 64 boundary elements in the shape of straight segments, evenly distributed with respect to the natural meridional coordinate of the elliptical coordinate system over the contours of the oblate spheroids, and an equal number of elements over the trace of the wall C_2 truncated at various levels, usually at $\sigma/a = 20$ or 30. In order to resolve the fine structure of the flow, the wall elements were concentrated around the axis. The ratio of lengths of the last wall element, away from the axis, to the first element, adjacent to the axis, was set equal to 30. These computations were followed by Richardson extrapolation with quadratic accuracy for improving the accuracy. A complete computation required approximately 30 s of CPU time on a SUN SPARCstation IPC.

In figure 2(*b–f*) we plot the resistance coefficients defined in (3.1), (3.2), and (3.3) for translation, rotation, and shear flow, reduced with respect to the corresponding coefficients for unbounded flow. The graphs are drawn with respect to either

particle–wall distance l/a or particle–wall spacing δ/a, and extend down to $\delta/a = 0.10$. Comparing the numerical results for the spherical particle, $a/b = 1$, to the analytical results tabulated by Goldman *et al.* (1967*a*, *b*), and the numerical results for $a/b = 2$ to the numerical results tabulated by Hsu & Ganatos (1989), we find agreement at least up to the fourth significant figure for all drag coefficients. These successful comparisons testify to the accuracy and efficiency of the present boundary integral formulation and numerical method of solution.

As the gap δ tends to zero, the resistance coefficients for translation and rotation F^T, T^T, F^R, T^R, exhibit singular behaviours, whereas those for shear flow F^S and T^S tend to obtain constant values. For a spherical particle, $a/b = 1$, the latter are in excellent agreement with the exact values 1.7005 and 0.94399 computed by Goldsmith *et al.* (1964*b*). As the aspect ratio a/b tends to infinity, the families of curves in the figures tend to limiting curves corresponding to a thin disk of infinitesimal thickness. The convergence to the thin-disk solutions is rapid for all drag coefficients except for T^S.

Hsu & Ganatos (1989) present extensive numerical data for the two aspect ratios $a/b = 2$ and 10, and our numerical results provide information for particles with intermediate shapes revealing some new features. First, we note that at large particle–wall spacings, the effect of aspect ratio has a noticeable but not drastic influence on all drag coefficients except for the torque coefficient T^S. Physically, this implies that the torque exerted on a particle that is held stationary in an incident shear flow increases dramatically as the particle obtains a more disk-like shape, thereby suggesting that the motion of flat particles, such as red blood cells, differ significantly from the motion of spheres.

Figure 2(*c*) shows that the curve for the torque coefficient T^T for a spherical particle shows a monotonic behaviour with positive values. The corresponding curve for $a/b = 1.10$ changes sign twice, at two different particle–wall spacings. At these positions, the torque exerted on a translating particle and the force exerted on a rotating particle are equal to zero. This implies that, under the action of a force directed along the y-axis, the particle will keep translating parallel to the wall without changing its orientation and thus, without exhibiting lateral motion. The curve for $a/b = 1.25$, on the other hand, shows a monotonic behaviour with negative values.

We thus find that there is a narrow window with respect to particle aspect ratio within which steady translation parallel to the wall is possible at two different particle–wall spacings. Nearly spherical particles and disk-like particles will rotate in opposite directions as they start translating parallel to a plane wall, and will tend to migrate in opposite directions as they start rotating around an axis that is parallel to the wall. To this end, it is interesting to note that the value of T^T exerted on toroidal particles is always positive (Kucaba-Pietal 1986), thereby demonstrating the importance of particle shape on the character of its motion.

4. Flow in a Hele-Shaw cell past a cylindrical post

To investigate the application of the present boundary integral method to channel flow, we consider pressure-driven flow in a Hele-Shaw cell past a cylindrical post illustrated in figure 3(*a*). This problem has a long history in fluid dynamics dating back to Hele-Shaw and Stokes (a review is given by Lee & Fung 1969). Recent interest was motivated by applications in pulmonary blood flow and flow within coating dies past arrested particles (Vrahopoulou 1992).

Our main goal in this section is to illustrate the formulation of the boundary integral

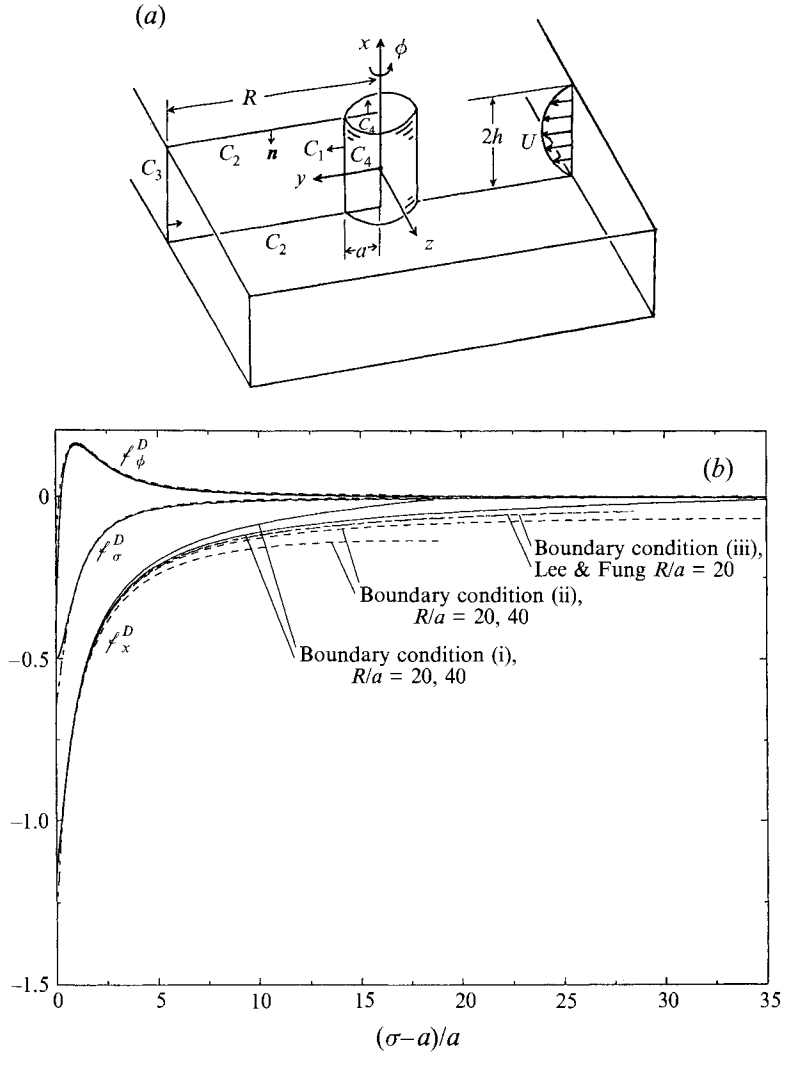

FIGURE 3. (*a*) Schematic illustration of plane Couette flow in a Hele-Shaw cell past a cylindrical post; (*b*) the distribution of the disturbance stresses along the upper wall for three types of far-field boundary condition and different levels of numerical truncation of the domain of flow.

method and discuss its numerical implementation. In a numerical method of solution, the infinite domain of flow must be truncated at a finite length, and the natural far-field boundary condition must be replaced by an approximate artificial boundary condition. We shall show that the choice of this condition has a negligible effect on the structure of the flow in the vicinity of the post, but has a first-order effect on the magnitude of the drag force exerted on the two plates.

In figure 3(*a*) we present a schematic illustration of pressure-driven flow in a Hele-Shaw cell of thickness $2h$ past a cylindrical post of radius a. In the absence of the post we obtain unidirectional plane Hagen–Poiseuille flow with velocity and pressure given by

$$u_y^P = U\left(1-\frac{x^2}{h^2}\right), \quad P^P = -Gy, \tag{4.1}$$

where $U = G/(2\mu h^2)$ is the centreline velocity, the constant $G = -\mathrm{d}P/\mathrm{d}y$ is equal to the negative of the undisturbed pressure gradient, and the superscript P stands for 'parabolic'. The no-slip and no-penetration conditions require that the velocity vanishes over the surface of the cylinder and the two walls.

Far from the cylinder, the disturbance flow due to the post behaves like the flow due to a point force whose strength is equal to the negative of the drag force exerted on the cylinder. This suggests that the disturbance velocity decays as $1/\sigma^2$ whereas the disturbance pressure decays as $1/\sigma$. These scalings suggest that the disturbance force exerted on the two plates is not equal and opposite to the drag force exerted on the post (Lee & Fung 1969).

4.1. *Boundary integral formulation and boundary conditions*

As a first step towards developing the boundary integral formulation, we express the flow in terms of a single-layer potential. We thus consider the disturbance flow due to the post, and select a control volume that is confined by the axisymmetric surfaces D_1, D_2, D_3, whose traces in the x, y-plane are the contours C_1, C_2, C_3 illustrated in figure 3(*a*). The collection of D_1, D_2, D_3 comprises the set S introduced in §2.

Applying the boundary integral equation (2.1) at a point x_0 that is located within the control volume, and noting that the disturbance velocity vanishes over D_2, we find

$$\boldsymbol{u}^D(\boldsymbol{x}_0) = -\frac{1}{8\pi\mu}\sum_{i=1,2,3} \boldsymbol{I}^s(\boldsymbol{x}_0;\boldsymbol{f}^D, D_i) + \frac{1}{8\pi}\sum_{i=1,3} \boldsymbol{I}^d(\boldsymbol{x}_0;\boldsymbol{u}^D, D_i). \tag{4.2}$$

The superscript D stands for 'disturbance'. The orientation of the normal vector, which is inherent in the single-layer and double-layer potentials, is depicted in figure 3(*a*).

Next, we consider the undisturbed parabolic flow $\boldsymbol{u}^P$ and apply the boundary integral equation (2.1) at the same point $\boldsymbol{x}_0$ using as control volume the interior of the cylinder, to obtain

$$-\frac{1}{8\pi\mu}\sum_{i=1,4} \boldsymbol{I}^s(\boldsymbol{x}_0;\boldsymbol{f}^P, D_i) + \frac{1}{8\pi}\boldsymbol{I}^d(\boldsymbol{x}_0;\boldsymbol{u}^P, D_1) = 0. \tag{4.3}$$

Here the superscript P stands for 'parabolic'. The normal vector in (4.3) points outside the cylinder, as shown in figure 3(*a*).

Adding the left-hand side of (4.3) to the right-hand side of (4.2) and taking into account that the total velocity over the surface of the cylinder must vanish, i.e. $\boldsymbol{u}^D + \boldsymbol{u}^P = 0$ over D_1, we obtain

$$\boldsymbol{u}^D(\boldsymbol{x}_0) + \frac{1}{8\pi\mu}\boldsymbol{I}^s(\boldsymbol{x}_0;\boldsymbol{f}^P, D_4)$$

$$= -\frac{1}{8\pi\mu}\boldsymbol{I}^s(\boldsymbol{x}_0;\boldsymbol{f}, D_1) - \frac{1}{8\pi\mu}\sum_{i=2,3} \boldsymbol{I}^s(\boldsymbol{x}_0;\boldsymbol{f}^D, D_i) + \frac{1}{8\pi}\boldsymbol{I}^d(\boldsymbol{x}_0;\boldsymbol{u}^D, D_3). \tag{4.4}$$

Now, we argue that as the radius R of D_3 tends to infinity, the corresponding double-layer potential makes a vanishing contribution, and the last term on the right-hand side of (4.4) may be discarded. We note, however, that this simplification is valid only when the integral equation is applied at a point $\boldsymbol{x}_0$ that is far from D_3.

Having developed the desired single-payer representation, we apply the Fourier

decompositions outlined in §2 to derive a set of three scalar integral equations for the Fourier vector $\not{f}$,

$$U_\alpha^D(x_0,\sigma_0)+\frac{1}{4\pi\mu}\int_{C_4}\Phi_{\alpha\beta}(x_0,\sigma_0,x,\sigma)\not{f}_\beta^P(x,\sigma)\,\sigma\,\mathrm{d}l(x)$$

$$=-\frac{1}{4\pi\mu}\int_{C_1}\Phi_{\alpha\beta}(x_0,\sigma_0,x,\sigma)\not{f}_\beta(x,\sigma)\,\sigma\,\mathrm{d}l(x)-\frac{1}{4\pi\mu}\sum_{i=2,3}\int_{C_i}\Phi_{\alpha\beta}(x_0,\sigma_0,x,\sigma)\not{f}_\beta^D(x,\sigma)\,\sigma\,\mathrm{d}l(x). \tag{4.5}$$

Using (4.1) we find that the Fourier vector $\not{f}^P$ over C_4 is given by

$$(\not{f}_x^P,\not{f}_\sigma^P,\not{f}_\phi^P)=\tfrac{1}{2}G(\sigma,-h,-h)\quad\text{at}\quad x=h,\quad(\not{f}_x^P,\not{f}_\sigma^P,\not{f}_\phi^P)=-\tfrac{1}{2}G(\sigma,h,h)\quad\text{at}\quad x=-h. \tag{4.6}$$

These expressions are used to evaluate the integral over C_4 on the left-hand side of (4.5) which thus becomes a known.

To complete the definition of the problem, we require boundary conditions for the velocity over the contours C_1, C_2, and C_3. Over the first two contours we stipulate that $\boldsymbol{u}^D=-\boldsymbol{u}^P$ and $\boldsymbol{u}^D=0$, respectively, to obtain

$$(U_x^D,U_\sigma^D,U_\phi^D)=[0,-u_y^P(x),-u_y^P(x)]\quad\text{over}\quad C_1,\quad \boldsymbol{U}^D=0\quad\text{over}\quad C_2. \tag{4.7}$$

The precise form of the boundary condition over the computational boundary C_3 is responsible for establishing the far-field behaviour of the flow and, therefore, for determining the magnitude of the drag force exerted on the two plates. We have implemented three types of far-field condition.

Condition (i): assuming that the radius R of C_3 is sufficiently large, we discard the integral over C_3 to obtain a system of integral equations for the Fourier coefficients $\not{f}$ over C_1 and for the disturbance Fourier coefficients $\not{f}^D$ over C_2.

Condition (ii): we maintain the integral over C_3 and require the boundary condition $\boldsymbol{u}^D=0$ over C_3 to obtain a system of integral equations for the Fourier coefficients $\not{f}$ over C_1 and for the disturbance Fourier coefficients $\not{f}^D$ over C_2 and C_3.

Condition (iii): we maintain the integral over C_3 and require a boundary condition for the disturbance velocity that derives from the asymptotic solution of Lee and Fung (1969). In our notation, this condition takes the form

$$(U_x^D.\,U_\sigma^D,U_\phi^D)=\frac{G}{2\mu}(h^2-x^2)\frac{a^2}{\sigma^2}\frac{K_2(A)}{K_0(A)}(0,1,-1) \tag{4.8}$$

over C_3, where $A=\pi a/(2h)$ and K_0 and K_2 are modified Bessel functions.

It should be noted that implementing the boundary condition (iii) is not entirely consistent with the boundary integral equation (4.5), for the double-layer potential over C_3 on the right-hand side of (4.4) has already been discarded. We shall see, however, that the numerical results obtained by using this condition are in excellent agreement with the series solution of Lee & Fung (1969). An explanation for this behaviour is that since both the disturbance velocity and Green's function for the stress decay as $1/\sigma^2$ far from the cylinder, as the radius R of D_3 tends to infinity, the contribution of the double-layer integral over C_3 on the right-hand side of (4.4) decays as $1/\sigma^3$. On the other hand, the disturbance pressure and Green's function for the velocity decay as $1/\sigma$ which implies that the contribution of the single-layer integral over D_3 to the right-hand side of (4.5) decays as $1/\sigma$. The faster decay of the double-layer potential compared to that of the single-layer potential renders the single-layer potential dominant as far as determining the far-field behaviour of the flow.

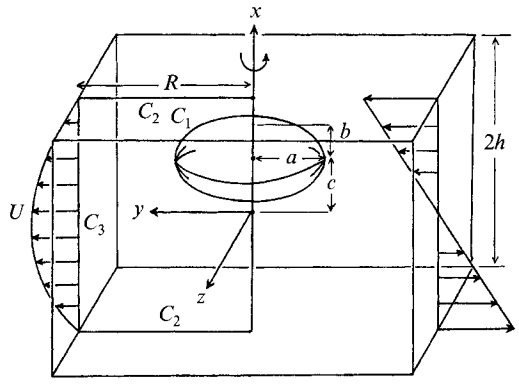

FIGURE 4. Schematic illustration of flow past an axisymmetric particle in a Hele-Shaw cell.

Far-field condition	R/a	f_W	f_C
(i)	20	3.896	4.919
	30	3.922	4.935
	40	3.931	4.940
(ii)	20	−1.311	4.984
	30	−1.316	4.964
	40	−1.340	4.957
(iii)	20	1.391	4.949
	30	1.377	4.949
Lee & Fung, two-term		1.362	4.963
Lee & Fund, exact (estimated)		1.320	4.938

TABLE 1. The drag coefficients on the upper plate and cylinder for various far-field conditions and radii of the computational domain of flow

4.2. *Results and discussion*

In figure 3(*b*) we plot the three components of the disturbance Fourier coefficient vector $\mathscr{f}^D$ over the trace of the upper plate for $h/a = 1$, computed using the far-field condition (i) with $R/a = 20, 40$; the far-field condition (ii) with $R/a = 20, 40$; and the far-field condition (iii) with $R/a = 20$. In the same figure we also show the predictions of the solution of Lee & Fung (1969) obtained by maintaining two terms in the exact series expansion, presented in the Appendix.

All numerical solutions agree well with each other in the vicinity of the cylinder, but show distinct far-field behaviour. The numerical solution with far-field condition (iii) shows excellent agreement with the two-term solution of Lee & Fung at large distances from the cylinder. The discrepancies near the cylinder are due to the inherent error from the two-term truncation. As the radius of the computational domain R/a is increased, all numerical solutions tend to the two-term solution of Lee & Fung.

In table 1 we present the dimensionless drag coefficients f_W and f_C defined on the basis of the equations $\boldsymbol{F}_W^D = -4\pi\mu U h f_W \boldsymbol{j}$ and $\boldsymbol{F}_C = -4\pi\mu U h f_C \boldsymbol{j}$, where $\boldsymbol{F}_W^D$ is the disturbance drag force exerted on the upper wall, $\boldsymbol{F}_C$ is the force exerted on the cylinder, and $\boldsymbol{j}$ is the unit vector in the y-direction. At the end of the table we also show the predictions of the exact and the two-term expansion of Lee & Fung presented in the Appendix. The exact values were computed from the approximate values taking into account a 0.5% error reported by Lee & Fung.

We observe that as R/a is increased, the drag coefficient f_C computed using the far-

field conditions (i) and (ii) tend to those predicted by the exact solution, and that the value of f_C computed using the far-field condition (iii) remains close to the exact value. Most rapid convergence is achieved by using the far-field condition (i). The drag coefficient f_W shows a notable sensitivity to the type of far-field condition, and may take either positive or negative values. The values of f_W computed using the far-field condition (iii) are in fair agreement with the analytical predictions of Lee & Fung.

Overall, the results of this section demonstrate the importance of domain truncation on the far-field behaviour of the flow and on the magnitude of the drag force exerted on the plates. More importantly for our purposes, they demonstrate the insensitivity of the flow in the vicinity of the cylinder to the nature of the far-field condition, and suggest using condition (i) for fastest convergence with respect to domain truncation.

5. Particle motion in the Hele-Shaw cell

Having considered the motion of particles in an infinite fluid, and having investigated the implementation of the boundary integral method to channel flow, we proceed to consider the motion of particles in a Hele-Shaw cell illustrated in figure 4. We are interested in computing the force and torque exerted on a particle that (*a*) translates or rotates in an otherwise quiescent fluid, or (*b*) is held stationary in the incident Couette flow $\boldsymbol{u}^\infty = (0, kx, 0)$ or Poiseuille flow described in (4.1). The drag coefficients for translation, rotation, and Couette flow were defined in (3.1), (3.2), and (3.3). For Poiseuille flow we introduce the additional coefficients F^P and T^P defined by the equations

$$\boldsymbol{F} = 6\pi\mu a u_y^P(x)\, F^P \boldsymbol{j}, \quad \boldsymbol{T} = 4\pi\mu a^3 \left(\frac{\partial u_y^P}{\partial x}\right)_{x=c} T^P \boldsymbol{k}, \tag{5.1}$$

where $x = c$ is the particle centre. When the size of the particle is small compared to the clearance of the channel, F^P and T^P reduce to the corresponding coefficients for shear flow in an unbounded fluid, with shear rate equal to the local slope of the velocity.

5.1. *Boundary integral formulations*

Considering the flow due to a particle that translates along the y-axis or rotates around an axis that passes through its centre and is parallel to the z-axis in an otherwise stationary fluid, we follow a procedure similar to that outlined in §3 to obtain the integral equation

$$U_\alpha(x_0, \sigma_0) = -\frac{1}{4\pi\mu} \sum_{i=1,2,3} \int_{C_i} \Phi_{\alpha\beta}(x_0, \sigma_0, x, \sigma) f_\beta(x, \sigma)\, \sigma\, \mathrm{d}l(x). \tag{5.2}$$

C_1 is the trace of the particle, C_2 is the trace of the walls, and C_3 is a numerical boundary that is located at $\sigma = R$ as shown in figure 4.

The boundary conditions on the particle surface were discussed in §3. Over the walls of the channel we require the no-slip and no-penetration conditions, yielding $\boldsymbol{U} = (0, 0, 0)$ at $x = \pm h$. Two choices for $\boldsymbol{U}$ over C_3 are provided by the far-field conditions (i) and (ii) discussed in §4. Physically, condition (i) corresponds to flow due a particle that moves between two circular disks or radius R immersed in a pool of stagnant fluid. Condition (ii) corresponds to the flow due a particle that moves in a circular Hele-Shaw cell of radius R which is sealed around the rim. For a sufficiently large radius R, using either condition yields virtually identical results for the drag force and torque exerted on the particle, as well as for the distribution of surface force over the particle surface.

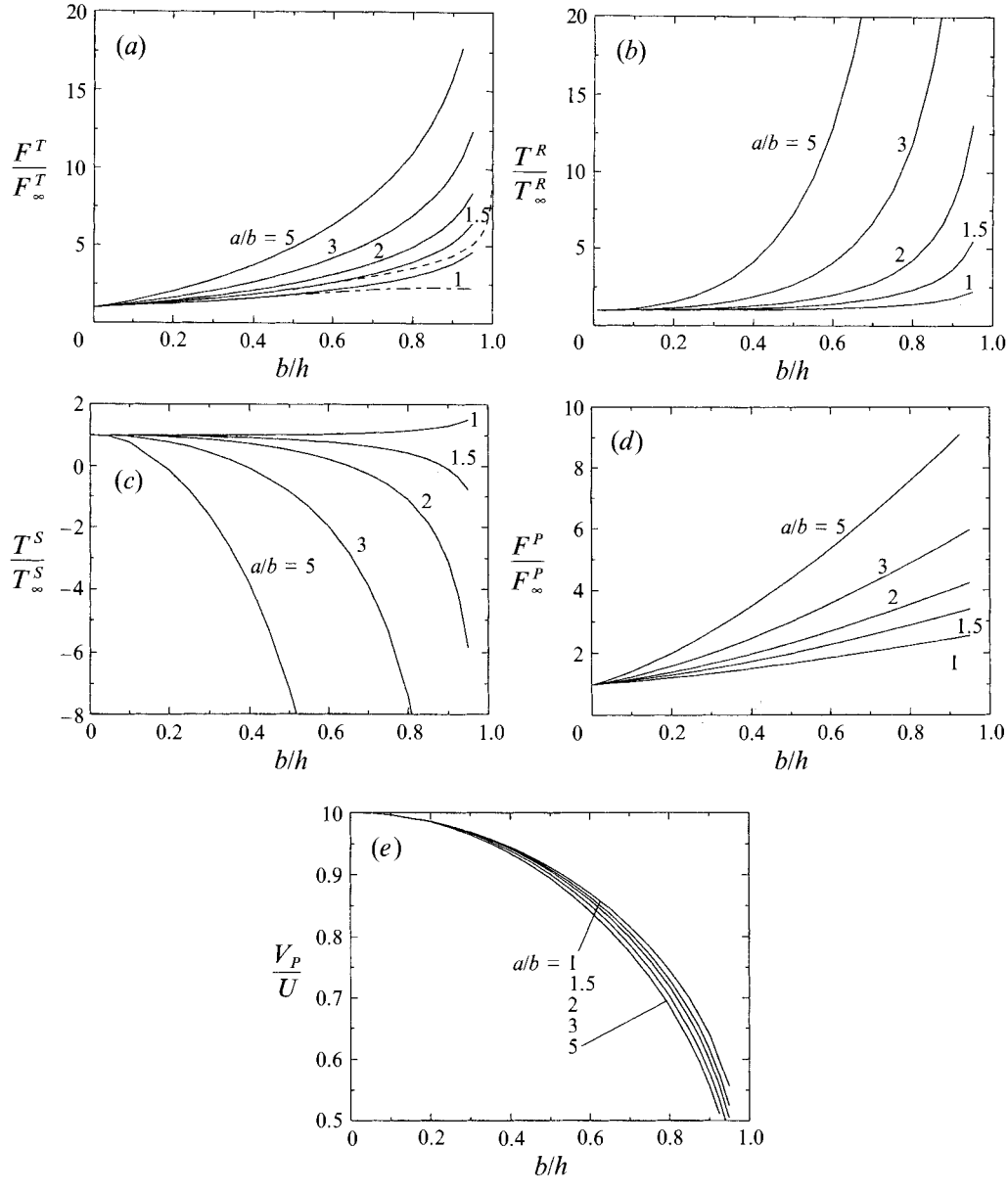

FIGURE 5. (*a–d*) Drag coefficients for translation, rotation, shear and parabolic flow, for oblate spheroids placed at the centre of the channel; the subscript ∞ designates the respective coefficients for infinite flow. (*e*) The convection velocity of freely suspended particles in Poiseuille flow normalized by the centreline velocity.

To describe the flow past a stationary particle, we follow the procedure of §4 to derive the boundary integral equation

$$U^D_\alpha(x_0,\sigma_0) = -\frac{1}{4\pi\mu}\int_{C_1} \Phi_{\alpha\beta}(x_0,\sigma_0,x,\sigma)\not{f}_\beta(x,\sigma)\,\sigma\,\mathrm{d}l(x)$$

$$-\frac{1}{4\pi\mu}\sum_{i=2,3}\int_{C_i} \Phi_{\alpha\beta}(x_0,\sigma_0,x,\sigma)\not{f}^D_\beta(x,\sigma)\,\sigma\,\mathrm{d}l(x), \quad (5.3)$$

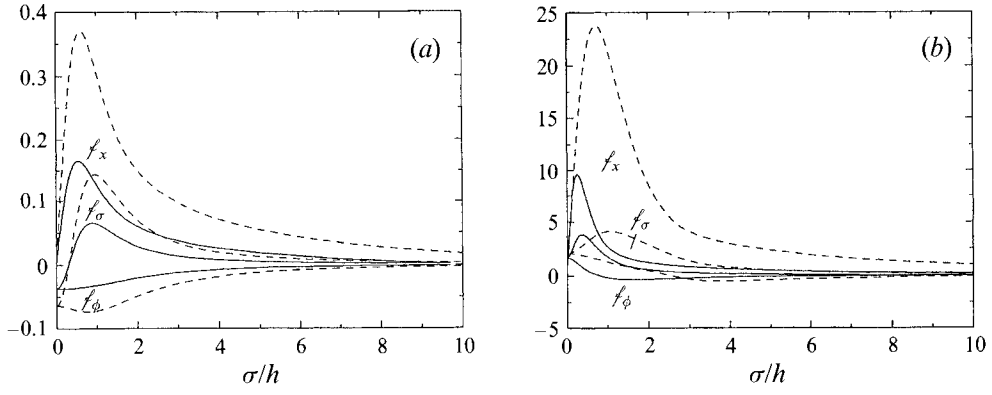

FIGURE 6. The distrubiton of the stresses along the upper plate due a spherical particle (solid lines) or a spheroidal particle with $a/b = 3$ (dashed lines) translating along the y-axis at the mid-plane of the channel, for particle sizes: (*a*) $b/h = 0.1$, (*b*) $b/h = 0.9$.

where the superscript D stands for 'disturbance'. The boundary conditions for the velocity over C_1 and C_2 are analogous to those given in (4.7). For a far-field condition we have the choice between (i) and (ii) discussed in §4.

The drag coefficients for shear and parabolic flow were computed using appropriate versions of (3.5), and the results were found to be in excellent agreement with those computed directly on the basis of (2.17) and (2.18), using the solution of (5.3).

5.2. *Results and Discussion*

We begin by considering particles located at the centreline of the channel, at $c = 0$. In figure 5(*a–d*) we plot the drag coefficients for several families of oblate spheroids of different sizes and aspect ratios, normalized with respect to the respective coefficients for unbounded flow. The drag coefficients that are not shown in the figures are equal to zero. We observe that as the size of the particles decreases, the effect of the walls becomes insignificant and all reduced drag coefficients tend to the value of unity. As the minor axis of the generating ellipse b tends to the semi-width of the channel h, and the clearance between the particle and the walls tends to zero, the drag coefficients for translation and rotation diverge, whereas the drag coefficients for shear and parabolic flow tend to constant values.

Concentrating on the curve for the spherical particle, $b/a = 1$, in figure 5(*a*), we compare the numerical results with the asymptotic predictions of Faxén applicable for small values of b/h indicated by the dash-dot line (quoted in Happel & Brenner 1983), and obtain a remarkably good agreement for particles of small and moderate size up to $b/h = 0.50$. For larger particles, the asymptotic predictions substantially underestimate the drag coefficients. Considering the opposite limit of tightly fitting particles at values of b/h close to one, we compare our numerical results to the predictions of the asymptotic theory of Goldman *et al.* (1964*a*) and O'Neill & Stewartson (1964) on the force and torque exerted on a spherical particle that translates parallel to a single plane wall. To account for the presence of both walls we simply multiply the asymptotic expressions by a factor of two. The numerical results follow the general trends indicated by the asymptotic solutions, but we observe a noticeable qualitative disagreement even at the smallest value of the clearance considered in the computations, $b/h = 0.95$. This behaviour is due to the slow logarithmic approach to the asymptotic limit.

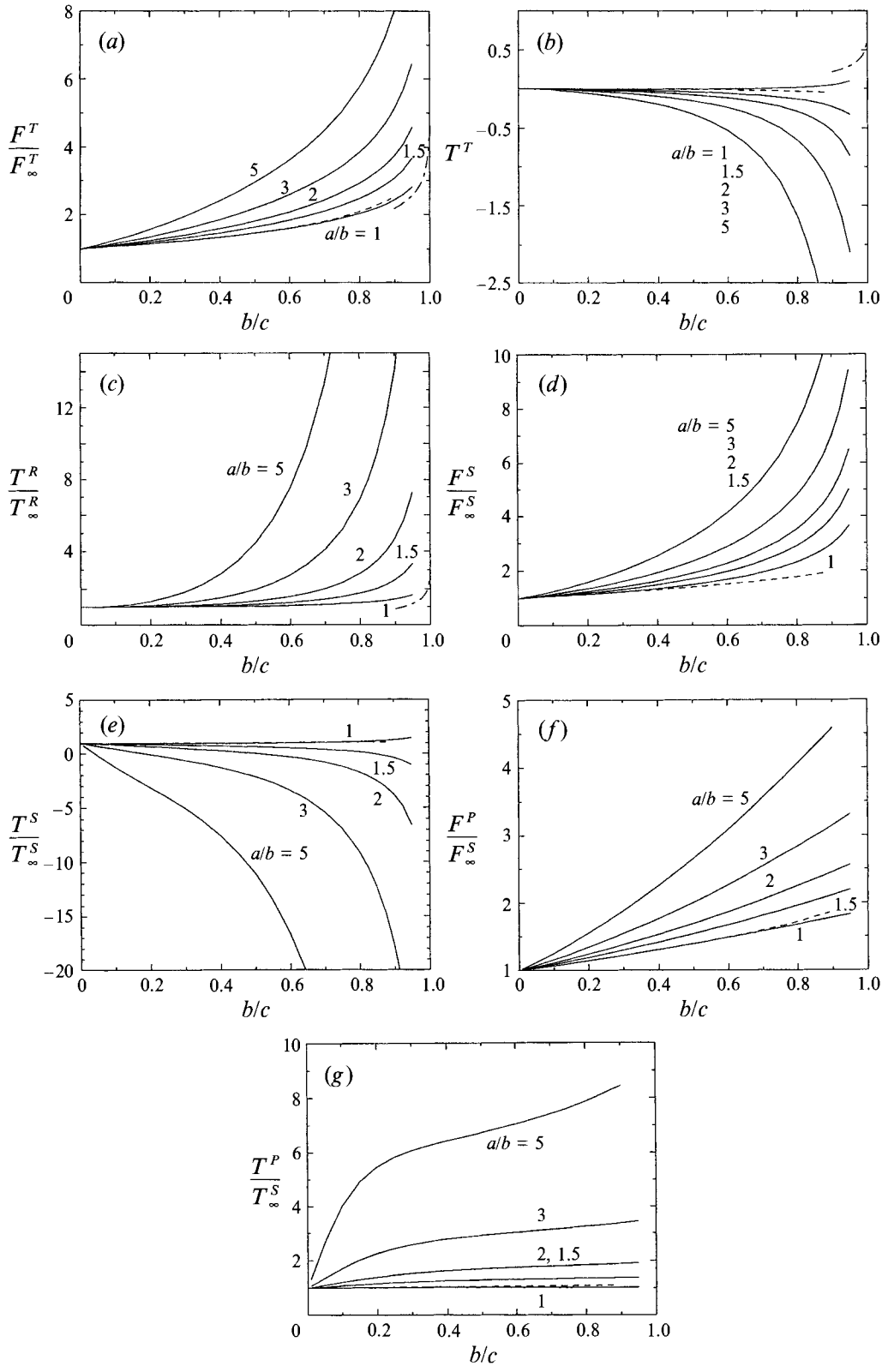

FIGURE 7. (*a–g*) Drag coefficients for translation, rotation, shear and parabolic flow, for oblate spheroids located off the centre of the channel at $c/h = 0.50$. The subscript ∞ designates the respective coefficients for infinite flow.

The strong dependence of the coefficient T^S on the particle size and aspect ratio is a striking feature of figure 5(*c*). For the spherical particle, T^S is positive irrespective of the particle radius. For non-spherical particles, as the particle size becomes larger, T^S changes sign at a critical value that depends on the aspect ratio a/b. This threshold value decreases rapidly as the particle aspect ratio is increased. Physically, these results imply that, under the action of a shear flow, small oblate spheroids will rotate in the direction indicated by the vorticity vector, whereas large oblate spheroids will rotate in the opposite direction. The later behaviour is due to the inhibiting action of the walls which is mediated through lubrication forces in the gaps between the particle and the walls. Given the particle aspect ratio, there is a critical particle size for sign reversal at which the particle will translate parallel to the walls without exhibiting rotation. The stability of this stationary motion requires further investigation.

In figure 5(*e*) we plot the ratio of the velocity of translation of a freely suspended particle V_p to the centreline velocity of the unperturbed Poiseuille flow U for several families of spheroidal particles with constant aspect ratio. Small particles are convected with nearly the centreline velocity, whereas tightly fitting particles are immobilized by strong lubrication forces at the points of minimum clearance. It is remarkable to observe that particles with $b/h = 0.50$, which fill half the channel width, translate at a velocity that is roughly 90% the unperturbed centreline velocity, for all aspect ratios. This behaviour was noted previously for spherical particles by Ganatos *et al.* (1982). For a given particle thickness b/h, the particle velocity decreases as the aspect ratio is increased, but only by a moderate factor.

To illustrate the effect of particle aspect ratio on the structure of the flow, in figure 6(*a*, *b*) we show the distribution of the stresses along the upper plate due to a translating spherical particle and a spheroidal particle with $a/b = 3$, for two different sizes, $b/h = 0.1$ and 0.9. These results are computed using the far-field condition (i). We note that in all cases, the pressure coefficient f_x tends to zero at the origin $\sigma = 0$, whereas the shear stress coefficients f_σ and f_ϕ obtain common finite values. The general features of the stress distributions for small particles, shown in figure 6(*a*), are insensitive to the particle aspect ratio; in both cases, the flow is similar to that generated by a point force located at the centre of the channel, oriented parallel to the walls, and with strength equal and opposite to the drag force exerted on the particles. The distributions of stresses for large particles, shown in figure 6(*b*), show a notable senstivity to aspect ratio in the vicinity of the particles, reflecting the onset of lubrication forces at the narrow gaps between the particles and the walls. Comparing the solid to the dashed curves in figure 6(*a*, *b*) we deduce that, given the particle aspect ratio, as the size of the particle is increased, the radial locations where the stresses attain maxima move inward, toward the particle axis, in order to accommodate the local lubricating flow.

We consider next particles that are located off the centre of the channel at the lateral position $c/h = 0.50$. In figure 7(*a*–*g*) we plot the resistance coefficients for translation, rotation, shear flow, and parabolic flow, and for several families of oblate spheroids. These coefficients are reduced with respect to the corresponding coefficients for infinite flow. The dashed lines show the predictions of Faxén and Wakiya for small spherical particles (quoted in Ganatos *et al.* 1980*b*), whereas the dot-dashed lines show the predictions of the lubrication theory of Goldman *et al.* (1964*a*, *b*), taking into account only the effect of the closest wall. The agreement between the numerical results and the asymptotic predictions of Faxén is excellent even for large particles, and we observe that the asymptotic theory of Goldman *et al.* (1964*a*, *b*) successfully captures the singular behaviour for small gaps. As the particle size is increased, and the gap between

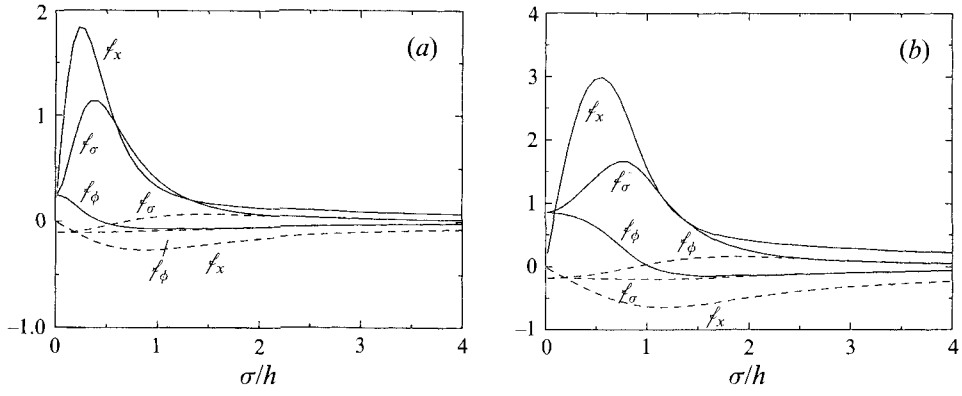

FIGURE 8. The distribution of stresses along the upper and lower walls (solid and dashed lines respectively) due to: (*a*) a spherical particle, and (*b*) a spheroidal particle with $a/b = 3$ translating along the y-axis at the elevation $c/h = 0.50$, for particle size $b/h = 0.50$.

the particles and the upper wall tends to close, the resistance coefficients for shear and parabolic flow tend to finite values that become larger as the particle aspect ratio is increased.

Comparing the present results for spherical particles to the corresponding numerical results tabulated by Ganatos *et al.* (1980*b*, table 3), we find general qualitative and quantitative agreement, but also occasional discrepancies. For instance, for $a/c = 0.50$ we find $F^S = 1.506$ and $T^S = 0.996$, while Ganatos *et al.* find $F^S = 1.420$ and $T^S = 1.023$. In spite of an exhaustive search, the reason for these discrepancies could not be identified.

The results shown in figure 7(*b*) indicate that both the sign and the magnitude of the torque exerted on a translating particle exhibit a strong dependence on the particle aspect ratio. Particles with a nearly spherical shape tend to rotate in the clockwise direction, whereas disk-like particles tend to rotate in the counterclockwise direction, just as they do when they move above a single plane wall (§3). Ganatos *et al.* (1980*b*) found that at $c/h = 0.50$, there is a critical radius of a spherical particle at which the particle translates without developing a torque and rotates without developing a force. Our results show that this critical size is $b/c = 0.65$, in rough agreement with the value read off the plots of Ganatos *et al.* To this end, we inquire whether, given the particle aspect ratio, there is a critical particle size for translation with zero torque or rotation with zero force. Figure 7(*b*) shows that this is feasible only for particles with a nearly spherical shape.

Concentrating on figure 7(*e*), we compare the numerical results to those shown in figure 5(*c*) for $c/h = 0$ and find similar trends, indicating that the behaviour of nearly spherical particles in a shear flow is distinctly different from that of flat particles, independently of the particle location across the channel.

To illustrate the effect of particle aspect ratio on the structure of the flow, in figure 8(*a*, *b*) we plot the distribution of stresses along the upper and lower walls due to a translating spherical particle and a spheroidal particle with $a/b = 3$. In both cases, the particles occupy half the clearance of the channel, $b/h = 0.5$. Solid lines correspond to the upper wall, and dashed lines correspond to the lower wall. One notable feature of the flow in the vicinity of the particle is the increased magnitude of the stresses on the upper wall compared to those on the lower wall. The general features of the stress distributions on the lower wall are quite insensitive to the particle aspect ratio, but

those over the upper wall show a significant dependence on the particle aspect ratio. The stress distributions on the upper wall are similar to those shown in figures 6(*a*, *b*) for motion along the centre of the channel. Far from the particle, the solid and dashed curves collapse as the distribution of stresses tend to become identical, but with a change in sign for the normal stress due to the opposite orientations of the normal vector.

This research is supported by the National Science Foundation, Grants CTS-9020728, CTS-9216176. Partial support was provided by the Department of Energy and the Exxon Education Foundation.

Appendix

We consider Poiseuille flow in the Hele-Shaw cell past a cylindrical post. Using the nomenclature of §§2 and 3 and the notation of figure 4, we find that the Fourier coefficients of the disturbance surface force along the upper plate, as predicted by the approximate two-term expansion of Lee & Fung (1969), are given by

$$f_x^D = -aG\frac{1}{2}\frac{a}{\sigma}\frac{K_2(A)}{K_0(A)}, \quad f_\sigma^D = -hG\frac{1}{2}\left[\frac{a^2}{\sigma^2}\frac{K_2(A)}{K_0(A)} - \frac{32}{\pi^3}\frac{h}{\sigma}\frac{K_2(k\sigma)}{K_0(A)}\right], \quad \text{(A 1), (A 2)}$$

$$f_\sigma^D = -hG\frac{1}{2}\left[\frac{a^2}{\sigma^2}\frac{K_2(A)}{K_0(A)} + \frac{16}{\pi^2}\frac{h}{\sigma}\frac{K_1'(k\sigma)}{K_0(A)}\right], \quad \text{(A 3)}$$

where $A = \pi a/(2h)$ and K_0 and K_2 are modified Bessel functions. The dimensionless drag coefficients on the cylindrical post and the walls are given by

$$f_C = \frac{a^2}{\sigma^2}\left[1 + \frac{K_2(A)}{K_0(A)} + \frac{16}{\pi^2}\frac{h}{\sigma ka}\frac{K_1(A)}{K_0(A)}\right], \quad \text{(A 4)}$$

$$f_W = f_D + \frac{a^2}{\sigma^2}\left[\frac{K_2(A)}{K_0(A)} - 1\right]. \quad \text{(A 5)}$$

REFERENCES

CLIFT, R., GRACE, J. R. & WEBER, M. E. 1978 *Bubbles, Drops, and Particles.* Academic.

DE MESTRE, L. J. 1973 Low-Reynolds-number fall of slender cylinders near boundaries. *J. Fluid Mech.* **58**, 641.

DVINSKI, A. S. & POPEL, A. S. 1987*a* Motion of a rigid cylinder between parallel plates in Stokes flow. Part 1: Motion in a quiescent fluid and sedimentation. *Comput. Fluids* **15**, 391–404.

DVINSKI, A. S. & POPEL, A. S. 1987*b* Motion of a rigid cylinder between parallel plates in Stokes flow. Part 2: Poiseuille and Couette flow. *Comput. Fluids* **15**, 405–419.

FUNG, Y. C. 1984 *Biodynamics, Circulation.* Springer.

GANATOS, P., WEINBAUM, S. & PFEFFER, R. 1980*a* A strong interaction theory for the creeping motion of a sphere between parallel boundaries. Part 1. Perpendicular motion. *J. Fluid Mech.* **99**, 739–753.

GANATOS, P., PFEFFER, R. & WEINBAUM, S. 1980*b* A strong interaction theory for the creeping motion of a sphere between parallel boundaries. Part 2. Parallel motion. *J. Fluid Mech.* **99**, 755–783.

GANATOS, P., WEINBAUM, S. & PFEFFER, R. 1982 Gravitational and zero-drag motion of a sphere of arbitrary size in an inclined channel at low Reynolds number. *J. Fluid Mech.* **124**, 27–43.

GOLDMAN, A. J., COX, R. G. & BRENNER, H. 1967*a* Slow viscous motion of a sphere parallel to a plane wall – I. Motion through a quiescent fluid. *Chem. Engng Sci.* **22**, 637–651.

GOLDMAN, A. J., COX, R. G. & BRENNER, H. 1967*b* Slow viscous motion of a sphere parallel to a plane wall – II. Couette flow. *Chem. Engng Sci.* **22**, 653–660.

HALPERN, D. & SECOMB, T. W. 1991 Viscous motion of disk-shaped particles through parallel-sided channels with near-minimal widths. *J. Fluid Mech.* **231**, 545–560.

HALPERN, D. & SECOMB, T. W. 1992 The squeezing of red blood cells through parallel-sided channels with near-minimal widths. *J. Fluid Mech.* **244**, 307–322.

HAPPEL, J. & BRENNER, H. 1983 *Low Reynolds Number Hydrodynamics*. Martinus Nijhoff.

HSU, R. & GANATOS, P. 1989 The motion of a rigid body in viscous fluid bounded by a plane wall. *J. Fluid Mech.* **207**, 29–72.

KIM, S. & KARRILA, S. J. 1991 *Microhydrodynamics, Principles and Selected Applications*. Butterworth–Heinemann.

KUCABA-PIETAL, A. 1986 Nonaxisymmetric Stokes flow past a torus in the presence of a wall. *Arch. Mech.* **38**, 647–663.

LEE, J. S. & FUNG, Y. C. 1969 Stokes flow around a circular cylindrical post confined between two parallel plates. *J. Fluid Mech.* **37**, 657–670.

LEE, J. S. & FUNG, Y. C. 1969 Stokes flow around a circular cylindrical post confined between two parallel plates. *J. Fluid Mech.* **37**, 657–670.

O'NEILL, M. E. & STEWARTSON, K. 1967 On the slow motion of a sphere parallel to a nearby plane wall. *J. Fluid Mech.* **27**, 705–724.

POZRIKIDIS, C. 1992 *Boundary Integral and Singularity Methods for Linearized Viscous Flow*. Cambridge University Press.

POZRIKIDIS, C. 1994 Shear flow over a plane wall with an axisymmetric cavity or a circular orifice of finite thickness. *Phys. Fluids* A, **6**, 1–12.

VRAHOPOULOU, E. P. 1992 Flow distortions around particles between parallel walls with application to streak formation in slide-coating methods. *Chem. Engng Sci.* **47**, 1027–1037.

WAKIYA, S. 1959 Effect of a submerged object on a slow viscous flow V. Spheroid at an arbitrary angle of attach. *Res. Rep. Fac. Engng Niigata Univ. Japan* **8**, 17–30 (in Japanese).

ZHOU, H. & POZRIKIDIS, C. 1993 The flow of suspensions in channels: Single files of drops. *Phys. Fluids* A **5**, 311–324.